Steady non-ideal detonations in cylindrical sticks of explosives

G.J. SHARPE and M. BRAITHWAITE[1]

School of Mathematics and Statistics, University of Birmingham, Birmingham, B15 2TT, UK (E-mail: sharpeg@ for.mat.bham.ac.uk); [1]*Royal Military College of Science, Cranfield University, Shrivenham, Swindon SN6 8LA, UK (E-mail: m.braithwaite@rmcs.cranfield.ac.uk)*

Abstract. Numerical simulations of detonations in cylindrical rate-sticks of highly non-ideal explosives are performed, using a simple model with a weakly pressure-dependent rate law and a pseudo-polytropic equation of state. Some numerical issues with such simulations are investigated, and it is shown that very high resolution (hundreds of points in the reaction zone) are required for highly accurate (converged) solutions. High-resolution simulations are then used to investigate the qualitative dependences of the detonation driving zone structure on the diameter and degree of confinement of the explosive charge. The simulation results are used to show that, given the radius of curvature of the shock at the charge axis, the steady detonation speed and the axial solution are accurately predicted by a quasi-one-dimensional theory, even for cases where the detonation propagates at speeds significantly below the Chapman-Jouguet speed. Given reaction rate and equation of state models, this quasi-one-dimensional theory offers a significant improvement to Wood-Kirkwood theories currently used in industry.

Key words: ANFO, detonation, explosives, numerical simulation, shock capturing

1. Introduction

Detonations are supersonic waves that can propagate through reactive materials which consist of a strong shock wave coupled to the exothermicty of the chemical reactions. In so-called non-ideal detonation processes, the non-linear coupling between front curvature and the details of the chemical decomposition kinetics is important in the propagation of the wave. The chemical physics of condensed phase non-ideal detonations is of relevance to a number of disparate industries, both from the point of view of safety and of performance. These include: (i) defence related industries where insensitive munitions (IMs) as well as low explosives used by terrorists entail non-ideal detonation processes; (ii) mining industry, where the modern commercial explosives used are mainly ammonium nitrate based water-in-oil emulsions or ammonium nitrate-fuel oil slurries (ANFO), sometimes incorporating ammonium nitrate prills (heavy ANFO, doped emulsions); (iii) industries where the manufacture, transport and storage of hazardous (explosive, combustible and detonable) materials are involved; (iv) chemical/petrochemical and fine chemical industries, where it is inevitable that some chemical processing operations will involve unstable intermediates, some of which may be detonable, these include those handling acetylene and acetylides, peroxides, nitrates and perchlorates, ethylene oxide and propylene oxide.

Theoretical attempts have been made to progress beyond simple one-dimensional thermo-hydrodynamic (Chapman-Jouguet) descriptions of condensed phase detonations in non-ideal explosives. One approach that is currently in use in the mining (*e.g.* [1]) and defence (*e.g.* [2])

industries is that based on Wood-Kirkwood theory [3], which uses a slightly divergent flow central stream tube approximation to give the solution only along the axis of a cylindrical charge. However, this is an incomplete theory which involves an unknown function (the axial flow divergence) that needs to be arbitrarily prescribed. Furthermore, there exist concerns over the validity of this slightly divergent flow approach for significantly non-ideal explosives, *e.g.* for determining critical diameters for detonations in different confinements (indeed, further unknown relationships between the radius of curvature of the shock at the axis, the charge diameter and confinement need to be empirically specified in this method in order to obtain detonation speeds as a function of diameter [1]).

A rational asymptotic theory for two-dimensional steady detonations is given in [4], based on the assumption of weak-shock curvature (on the detonation reaction-zone length) or equivalently on the assumption of detonation speed close to the Chapman-Jouguet (planar) detonation speed. Stemming from this work, there is now a large body of theoretical and experimental work on propagation laws of curved detonation fronts known as detonation shock dynamics (DSD) (see the review in [5], and references contained therein).

The lowest order asymptotic DSD theory is equivalent to an assumption that the front is quasi-one-dimensional and hence that it is governed by a single normal detonation speed-shock curvature (D_n–κ) law. This D_n–κ law can found from an asymptotic (small curvature) analysis (*e.g.* [4,6]) or numerical integration of the quasi-one-dimensional equations (*e.g.* [7,8], Short and Sharpe, submitted) given a reaction rate law and equation of state model. Applied to the ratestick problem, the asymptotic theory gives an equation which determines the shock shape of the steady-state detonation, which can then be used to solve the complete problem (*e.g.* detonation speed versus charge diameter) [4]. The shock-shape equation is subject to a boundary condition at the charge edge, which depends on the explosive and confinement model pair (this condition can be determined through a modified inert shock polar analysis at the shock-charge edge intersection point [5,9]). However, such an asymptotic theory based on small curvature/small detonation speed deficits from CJ is not likely to be valid for the highly non-ideal explosives of interest here, in which detonations can propagate even when the detonation speed is ∼50% of CJ and the shock front is strongly curved.

Indeed, it is found that the first-order DSD theory does not do well in describing experimental shock shapes for these highly non-ideal explosives. The experimentally measured shock shapes give a D_n–κ relation for the shock front as one moves from the charge axis to the charge edge. For mildly non-ideal explosives, such as PBX 9502 or Nitromethane, the D_n–κ relations along different shock fronts (*e.g.* corresponding to different charge diameters) do all lie close to one another or overlay, at least for sufficiently small curvatures [10–12], indicating that the dynamics of curved detonation fronts in such explosives are, to leading order, well described by a single D_n–κ law as predicted by the first-order theory. Indeed, the D_n–κ law determined from rate-stick experiments for a given explosive can then be used to theoretically determine the shock front dynamics for the explosive in more complex geometries [5, 13]. For the more non-ideal explosives, however, such as PBXN 1111 and ANFOs, the D_n–κ relations along individual shock fronts lie along different curves for different diameters, and these curves do not intersect or overlap [11,14,15]. Hence for these non-ideal explosives, the front propagation cannot be described a simple, single D_n–κ law such as the first-order DSD theories give, and thus higher order (two-dimensional) effects must be important.

A second-order (in the deficit of the detonation speed from CJ) DSD theory exists [5,13, 15]. At second order, two-dimensional (and time-dependent) effects and brought into play. The D_n–κ relations along different shock fronts determined from this higher-order theory are in better qualitative agreement with the non-ideal explosive experiments. However, this

higher-order theory is still based on the rational asymptotic limit that the detonation is asymptotically close to the CJ speed. Hence it is not quantitatively predictive for highly non-ideal explosive such as heavy ANFOs and doped emulsions in which the departure from the CJ speed is significant. Furthermore, to date this theory has only been developed for a specific, simple form of the reaction-rate law, with a square-root dependence on the reaction progress variable (square-root depletion), a polytropic equation of state and only for slab geometry. The analysis would be significantly less tractable for more complex forms of the reaction-rate model (note that even changing from square root to simple depletion (a linear dependence of the rate law on the reaction progress variable) introduces logarithmic near-sonic boundary layers, even in the first-order DSD theory [16]), as well as for cylindrical-charge geometry due the introduction of geometric source terms.

In order to increase the range over which the higher order theory is valid, an extended theory based on the exact shock-change equation is also given in [13], where the single unknown term in the equation is approximated using the higher-order DSD theory results. For lower detonation speeds, this extended theory gives results which are significantly different to the higher DSD theory (J. Bdzil, private communication), and which are in much better agreement with the results for front shapes and speeds from numerical simulations [13]. However, this shock-change equation based theory is essentially only a front-propagation law, and one cannot reconstruct the flow field behind the shock (*e.g.* along the charge axis or the explosive-inert interface) from this, since the equation on which it is based is valid only at the shock. Furthermore, this front-propagation theory has again only been developed for the simple pressure-dependent rate law with square-root depletion and a polytropic equation of state in slab geometry.

Hence in order to investigate highly non-ideal steady detonations in cylindrical charges, including the details of the reactive flow field in the reaction zone and detonation products, one must currently resort to direct numerical simulations of the full reactive Euler equations. Aslam and co-workers [5,9,13,15] performed several simulations in two-dimensional slab geometry. Their main interest was in validating or comparing with various aspects of DSD theory. However, a major result of this work was to show that for reasonably accurate results, numerical resolutions of more than about 50 numerical grid points in the reaction-zone length are required [13]. Importantly, this raises severe questions regarding the validity of engineering style calculations, which typically only use 4–10 grid points in the reaction zone (*e.g.* [17]). Axisymmetric simulations of cylindrical charges were performed in [18]. They found that for small charge diameters the sonic locus in the steady-state wave could be different to that in the analysis in [4]. However, the calculations were less accurate than those of Aslam and co-workers, and they only presented results for two (unconfined) cases. Some simulations in slab geometry have also been performed in [19], but were interested only in comparing numerical methods, rather than in the details of the solution. Hence parametric studies of detonations in cylindrical charges using high-resolution simulations are needed.

In this paper we perform such high-resolution studies of non-ideal detonations in cylindrical charges for a simple reaction rate law and equation of state. The purpose of the paper is threefold: (i) to provide complete two-dimensional solutions which can be used for assessing and improving approximate theories (*e.g.*, we use the results to show that a significant improvement to Wood-Kirkwood theory for determining the axial solution is provided by a quasi-one-dimensional theory); (ii) to investigate how the qualitative nature of the reaction-zone structure changes with charge diameter and with the degree of confinement; (iii) to examine and identify some numerical issues that arise in such simulations, even when simple models are used. We stress here at the outset that this paper is not concerned with modelling

of a specific explosive, nor in detailed modelling of reaction rates or equations of states for such explosives, nor in explicit modelling of the heterogeneities inherent in many non-ideal explosives. Finally, here we are concerned only with the steady-state solutions, and not in the evolution to this steady state.

2. The model

The governing equations of the model are the Reactive Euler equations, which represent conservation of mass, momentum and energy coupled to a chemical reaction,

$$\frac{D\rho}{Dt} + \rho\nabla\cdot\mathbf{v} = 0, \quad \rho\frac{D\mathbf{v}}{Dt} = -\nabla p, \quad \frac{De}{Dt} - \frac{p}{\rho^2}\frac{D\rho}{Dt} = 0, \quad \frac{D\lambda}{Dt} = W, \quad \left(\frac{D}{Dt} = \frac{\partial}{\partial t} + \mathbf{v}\cdot\nabla\right). \quad (1)$$

Here $\mathbf{v}$ is the material velocity, ρ is the material density, p the pressure, e the internal energy per unit mass, λ a reaction progress variable (*i.e.*, $\lambda = 0$ in the initial explosive and $\lambda = 1$ in the completely burnt state), with W the reaction rate.

Equations (1) are closed by specifying an equation of state (eos) and a form for the reaction rate. For the purposes of the paper as stated in the introduction, it is sufficient to use relatively simple, but representative, eos and rate laws. Note first that theoretical detonation curvature studies show that highly non-ideal detonations, which can propagate even when the front curvature is large and at speeds which depart significantly from the CJ speed, are associated with rate laws which are not very state sensitive (*e.g.* [8,15, Short and Sharpe, submitted]). While the main results here are generic to non-ideal explosives, the rate and eos laws that are used were chosen to be representative of commercial ANFO explosives, namely

$$e = \frac{p}{(\gamma^* - 1)\rho} - Q\lambda, \quad \gamma^* = \gamma_0 + \gamma_1\frac{\rho}{\rho_0} + \gamma_2\frac{\rho^2}{\rho_0^2}, \quad (2)$$

where Q is the heat of reaction and ρ_0 is the initial density of the explosive, and

$$W = \frac{1}{\tau}\left(\frac{p}{p_{\text{ref}}}\right)^{(1.5)}(1 - \lambda), \quad (3)$$

where

$$\gamma_0 = 1.3333, \quad \gamma_1 = 0.36264, \quad \gamma_2 = 0.076288, \quad p_{\text{ref}} = 1\,\text{GPa},$$

$$Q = 3.822 \times 10^6\ \text{J kg}^{-1}$$

Hence a simple pseudo-polytropic eos given in Equation (2) is used to represent the thermodynamics of the explosive and its detonation products (*cf.* [1]). This eos and its associated parameters are chosen to give a match for adiabatic γ at both the CJ state and in the hot gaseous products to those determined from an ideal (thermochemical equilibrium) detonation code, which is based on a fundamental intermolecular potential based equation of state for the fluid state [20].

Note that for this eos the sound speed, c, is defined by

$$c^2 = \left[\frac{p}{\rho^2} - \left(\frac{\partial e}{\partial\rho}\right)\right]\left(\frac{\partial e}{\partial p}\right)^{-1} = \frac{\gamma^* p}{\rho} + \left(\frac{\gamma_1}{\rho_0} + 2\gamma_2\frac{\rho}{\rho_0^2}\right)\frac{p}{(\gamma^* - 1)}. \quad (4)$$

and adiabatic γ is then given by

$$\gamma = \frac{\rho c^2}{p}.$$

The 1·5 power for the pressure dependence in the reaction rate was chosen from a best fit of the results from an industrial Wood-Kirkwood code with experimental data (I. Parker, C. Cunningham, private communications), while the value of the rate constant is taken to be

$$\tau = 28 \ \mu\text{s},$$

which was chosen so that the detonation speed determined from the numerical simulations agreed well with the experimental result for the case of an unconfined explosive with a charge diameter of 100 mm.

Note that our choice of rate law and eos can be considered one of a commonly used class of models with pressure-dependent rate laws of the form $k p^n (1 - \lambda)^m$ (k a rate constant) and equations of state of the form $e = p / ((\gamma^* - 1)\rho)$, as used in previous rate-stick simulations (the case $n = 0$, $m = 1/2$, $\gamma^* = \gamma = 3$ was considered in [19], results for $n = 1$, $m = 1$, $\gamma^* = \gamma = 1·4$ were given in [18], while Aslam and co-workers [5,9,13,15] used $m = 1/2$, $\gamma^* = \gamma = 3$ and $n = 0, 1, 2$ and 3). Some additional results with a different choice of the eos and rate parameters are given in the Appendix A, which shows that the main results and conclusions described in Section 5 below are not sensitive to the choice of parameters for this class of models. Note also that even the more complex, semi-empirical rate laws often used to model specific explosives (*e.g.* [1]) are essentially pressure-dependent rates.

For our choice of model parameters, we also fix the initial pressure and density of the explosive, p_0 and ρ_0 respectively, to be

$$p_0 = 1 \times 10^5 \ \text{Pa}, \quad \rho_0 = 0·8 \ \text{g/cm}^3.$$

Here we are concerned with detonations in cylindrical rate sticks, and therefore solve the two-dimensional, axially symmetric version of Equations (1), *i.e.,* in (r, z) co-ordinates. The material velocity is then $\mathbf{v} = (u, w)$, where u and w are the radial and axial components, respectively.

We also need to model the effects of different confinements. In this work we are concerned with how the confinement affects the detonation wave in the explosive, rather than in the motion of the confinement. Hence in order to model confinement we simply include an inert material surrounding the explosive which has the same properties as the explosive itself (apart from being non-reactive), *i.e.*, the inert is taken to have an equation of state as in the explosive, given by the first term in the definition of e in Equation (2). Since the explosive and confining inert are in mechanical equilibrium, the initial pressure of the confining inert is equal to that in the explosive (1×10^5 Pa). Increasing confinement effects can then be modelled by varying the initial density of the inert, ρ_I. While simple, this model allows us to consider all cases from completely unconfined ($\rho_I \to 0$, for which the inert then behaves as an ideal gas) to infinite confinement ($\rho_I \to \infty$, for which the inert behaves as a solid, immovable wall). Also, from a numerical perspective, this is very efficient since it allows us to solve the whole system (explosive and inert) as a single material with the interface numerically captured, and hence this avoids unresolved numerical and closure issues involved in tracking and keeping a sharp interface between the explosive and inert, which is required when the inert material has markedly different properties to that of the explosive. Note that [18] and [19] used the same approach for modelling confinement.

Hence the remaining parameters to vary are the charge diameter, d, and the initial density of the confining inert, ρ_I. In order to explore the effects of both charge diameter and confinement several cases were considered, for which d and ρ_I are given in Table 2.

3. Numerical method

To perform the numerical simulations in this paper we use the hierarchically adaptive grid code, Cobra, which has been developed for industrial applications by Mantis Numerics Ltd., and is described more fully in [21]. To summarize, it is a second-order Godunov (shock capturing) scheme, which employs a hierarchical series of grids $G^0, \ldots, G^N$, such that the grid G^n has mesh spacing $h/2^n$, where h is the mesh spacing on the base grid G^0. The higher grids only occupy regions where increased resolution is required. Refinement of the grids is controlled by comparing the solutions of each physical variable, and also their rates of change, on grids G^n and G^{n-1}. For detonation calculations we also ensure that the whole reaction zone is also refined to the highest grid, by forcing grid refinement whenever the size of the reaction rate is above some small value. This grid adaptivity makes the code particularly suitable for detonation simulations, where high resolution is required in the detonation reaction zone, but this reaction zone usually occupies only a very small part of the explosive.

The numerical domain is rectangular in (r, z) co-ordinates. The explosive initially lies in the region $r \leq d/2$, with the surrounding inert initially in the region $d/2 < r \leq R$, where R is the width of the domain in the radial direction. The boundary condition at $r = 0$ is a symmetry condition, while an outflow boundary condition was used at $r = R$, as in [18]. The thickness of the inert in the domain was 50 mm for all cases, *i.e.*, $R = d/2 + 50$. Outflow/inflow boundary conditions were also used at the boundaries in the z-direction.

In this study we are interested only in the steady propagation of the detonation through the explosive. Hence the initial conditions for the calculations were chosen so that the steady state was reached as quickly as possible in the simulations. After some experimentation it was found that this was achieved by initializing the calculations by placing the steady, planar ZND detonation wave onto the grid in the explosive region $r \leq d/2$, with the shock initially lying along $z = 0$ and the reaction zone lying in the region $z < 0$. Figure 1 shows profiles of pressure and λ in the ZND (plane) detonation. The detonation speed, shock pressure, CJ pressure (the pressure at the sonic point at the end of the reaction zone) and the 99% reaction length (the distance between the shock and the point where $\lambda = 0.99$) for the ZND detonation
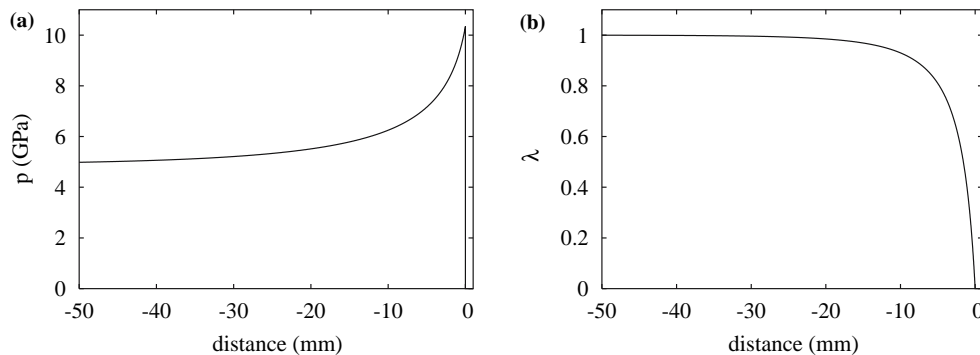

Figure 1. (a) Pressure and (b) reaction progress variable against distance behind the shock in the plane ZND detonation.

are

$$D_{CJ} = 4 \cdot 797 \text{ km/s}, \quad p_{shk} = 10 \cdot 3 \text{ GPa}, \quad p_{CJ} = 4 \cdot 88 \text{ GPa}, \quad l_{99} = 23 \cdot 1 \text{ mm}.$$

Note that the simulations are performed in the rest frame of the initial explosive, so that the detonation propagates through the numerical grid in the positive z-direction. The left (rear) z-boundary was placed sufficiently far (160 mm) behind the initial shock position so that it had little effect during the time of the simulations, while the right z-boundary was placed 800 mm ahead of it. The calculations were run until the detonation became steady in its own rest frame, *i.e.*, when its speed and reaction-zone structure became independent of time. Once the steady state was achieved, the results were transformed back into the rest frame of the detonation. Hence note that for all the results below, the axial material velocity corresponds to the shock rest-frame measured velocity, while the z-coordinate is the axial distance from the position of the shock front at the axis.

In the simulations presented here, the interface is captured and hence becomes smeared across a few grid cells behind the shock. Since we are using a conservative scheme and considering a single fluid (same eos in explosive and inert), the flow variables on either side of the captured interface should be correct provided the resolution is sufficiently high such that its numerical thickness is much thinner than any other length scale in the problem. This is a standard approach (*cf.* [18, 19]). The thickness of the captured interface can be seen in the density contour plots in Figure 4, which shows that in the detonation driving zone (DDZ, the part of the solution which can affect the front propagation) the captured interface remains very thin on the reaction-zone scale. In order to determine the 'location' of the interface, an advecting scalar is also tracked in the numerics which is initially unity in the explosive and zero in the inert. The interface 'locus' plotted in the figures in this paper are the contours where this scalar is equal to a half.

4. Numerical resolution study

An important numerical question is how much resolution is required to obtain well converged numerical solutions for the steady-state non-ideal detonation problem? While engineering-style calculations often use just a few (of the order of 10 or less) numerical grid points in the reaction zone [17], Aslam and co-workers [5, 13, 15] found that at least about 50 points in the reaction zone were necessary for reasonably accurate detonation speeds for their model. This is not surprising since the steady-state non-ideal detonation is essentially an eigenvalue problem, *i.e.*, the speed and structure of the wave are non-linearly coupled.

Here we are interested in the full solution of the two-dimensional DDZ (*e.g.*, shock shapes, axial solution, etc.), and it is therefore important to perform numerical resolution studies in order to ensure that the full numerical solution (not just the axial detonation speed) is well converged for non-ideal detonation problems. Furthermore, such a study is also useful in identifying and determining the effects of numerical artifacts inherent in shock capturing schemes on the non-ideal detonation solution (see below).

Table 1 shows the dependence of the solution along the charge axis on the numerical resolution for the case $d = 100$ mm, $\rho_I = \rho_0 = 0 \cdot 8$ g/cm^3. Here Δ is the grid spacing on the finest grid, which covers the reaction zone, l_{DDZ} is the non-ideal axial DDZ length (*i.e.*, the distance between the shock and sonic locus along the charge axis) in the steady state (14·9 mm in this case), p_{shk} is the shock-pressure at the axis. Note that we are using a shock-capturing scheme, as is the case for all previous simulations of the ratestick problem, which means that the shock is spread over a few numerical grid points, with the majority of the pressure rise

Table 1. Properties of axial solution as a function of numerical resolution for $\rho_I = 0.8 \, \text{g/cm}^3$ and $d = 100 \, \text{mm}$. Δ is the numerical grid spacing in the reaction zone, points/l_{DDZ} is the number of grid points between the shock and sonic loci along the charge axis, D is the detonation speed in the axial direction, p_{shk} is the numerical shock pressure on the axis, λ_{shk} is the amount of burning within the numerically smeared shock on the axis.

Δ (mm)	points/l_{DDZ}	D (km/s)	p_{shk} (GPa)	λ_{shk}
0·1	149·0	3·13	4·32	0·05
0·2	74·5	3·12	4·24	0·09
0·4	37·3	3·10	4·11	0·12
0·8	18·7	3·05	3·88	0·15
1·6	9·3	3·01	3·67	0·21
3·2	4·7	2·93	3·25	0·52

over 2 to 3 grid points. Since the rate is maximum just behind the shock in these types of reaction models, there will also be some burning occurring in the captured shock (*cf.* [18]), *i.e.*, the smeared shock and reaction overlap to some extent in the numerical solution. Hence also given in Table 1 is the value of the reaction progress variable at the axis at the point where the pressure is a maximum, λ_{shk} (*i.e.*, the degree of burning that occurs in the numerical shock). As the resolution increases and the shock becomes thinner, particles spend less time in the shock and hence this effect is decreased. However, one important ramification of this is that the normal speed of the wave in the simulation is not related directly to the numerically calculated shock pressure through the inert shock jump conditions, because some heat release has also occurred in the numerical shock. Indeed, this burning in the shock lowers the peak pressure for a given value of D. Hence in order to determine D, once the wave has reached steady state in the simulations (typical taken to be once the axial numerical shock pressure has stopped decreasing), the detonation is allowed to propagate further over many reaction times (until it is near the right z-boundary) and the speed determined by the distance it has propagated in this time of steady propagation.

There is also a further numerical effect acting (and interacting with the burning within the shock) which results in a lower apparent shock pressure. For simple pressure-dependent rate laws as used here, the pressures profiles have a well defined von Neumann spike, as in Figure 1. When such spiky profiles are discretized and averaged over a grid cell, the spike is 'clipped' resulting in a lower numerical shock pressure than in the exact solution. The amount of shock 'clipping' that occurs depends on the location of the physical spike with respect to the cell centre.

Returning to Table 1, we see that for our highest resolution of 0·1 mm (or about 150 points in the axial DDZ), the detonation speed is well converged, and less than 5% of the burning occurs within the numerical shock structure. The shock pressure is less well converged than the wave speed because of the well defined von Neumann spike, so that extremely high resolution would be required to prevent significant shock clipping. As the resolution decreases and drops below about 50 points/l_{DDZ}, the solution quickly degrades. For resolutions typically used in engineering calculations (*e.g.* the lowest two resolutions in Table 1), the numerical detonation speed and shock pressures are significantly below the converged values, while a large amount of the burning actually occurs within the numerical shock (over 50% for five points in the reaction zone).

Figure 2 shows the convergence of the shock pressure variation from the charge axis to the edge with numerical resolution. The lower the resolution, the more the shock pressure is underestimated across the entire charge diameter, as well as at the axis. However, note the numerical oscillations in the shock pressure with radius, and that the amplitude and wavelength of these oscillations decrease as the resolution increases. This is due to shock clipping, with the amount of clipping being dependent on the relative position of the von Neumann spike with respect to the cell centre, and the alignment of the shock with the grid. Such shock-pressure oscillations are inherent in shock-capturing schemes; indeed, very similar oscillations can be seen in Figure 7 of [18], which have relatively large amplitude due to the low resolutions used in that work.

With regard to the shock shape, any measure of the captured shock position in the numerics can of course only be at best accurate to within one numerical grid cell. Here we take the shock 'position' for a given r to be the cell in which the pressure is a maximum in the z-direction. Figure 3 shows the numerical shock loci for various resolutions. Clearly, very high resolution is also required to obtain a good representation of the shock shape on the grid. Note that it is difficult to determine local curvatures and shock normal angles from the data due to the finite resolution, in that on the grid scale the shock can look locally flat (this is especially true for engineering style resolutions, *e.g.*, Figure 3(d)). This is also an issue with experiments, due to the finite resolution of experimental techniques for measuring shock shapes [10, 12]. Note that the radial positions at which the numerical shock location jumps to lower axial cell positions in Figure 3 correspond to the positions of the local minimums in the shock pressure oscillations in Figure 2.

Our approach for determining the shape and local curvatures is to fit a curve through the data, as is done for experimental shock shapes [10–12]. However, there is still some ambiguity in the fit due to the local flatness of the data, but the error in the fit decreases with resolution. On the other hand, for lower resolutions, it can be seen that it would be very difficult to accurately determine the shock shapes.

In this paper we use a resolution of $\Delta = 0 \cdot 1$ mm throughout. A significantly higher resolution would be computationally prohibitive, even with our adaptive code. As can be seen above, this resolution is sufficient to obtain well converged solutions, at least for unconfined and lightly confined charges. However, as the confinement (ρ_I) increases, the shock front becomes flatter, and hence the shock shape and curvature become less well represented on the grid for a fixed resolution. Also, as ρ_I increases (for fixed diameter) the detonation speed and hence shock pressures increase, resulting in a higher reaction rate in the cells near the peak pressure and thus more shock burning and clipping for a fixed resolution. Hence even though our resolution of $\Delta = 0 \cdot 1$ mm, which corresponds to at least 149 points/l_{DDZ} (depending on confinement), is, as far as we are aware, the highest resolution of ratestick simulations published so far (in terms of points per reaction-zone length), some caution must still be attached in considering the very highly confined simulations as being well converged solutions.

5. Results

Consider first a 'base case' with $d = 100$ mm and $\rho_I = \rho_0 = 0 \cdot 8$ g/cm^3, for which the speed of the steady state detonation in the axial direction is $3 \cdot 13$ km/s (or $0 \cdot 652 D_{CJ}$). Figure 4 shows the pressure, density and reaction progress variable for the steady-state detonation in this case. Figure 5 shows the position of the shock, sonic locus and the explosive-inert interface. The
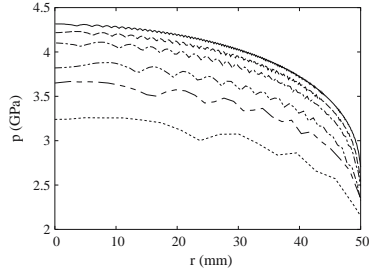
Figure 2. Numerical shock pressure versus radial position for $\rho_I = 0\cdot8\,\text{g/cm}^3$, $d = 100\,\text{mm}$ and numerical resolutions $\Delta = 0\cdot1\,\text{mm}$ (solid line), $0\cdot2\,\text{mm}$ (dashed line), $0\cdot4\,\text{mm}$ (dot-dashed line), $0\cdot8\,\text{mm}$ (double-dot-dashed line), $1\cdot6\,\text{mm}$ (triple-dot-dashed line) and $3\cdot2\,\text{mm}$ (dotted line).
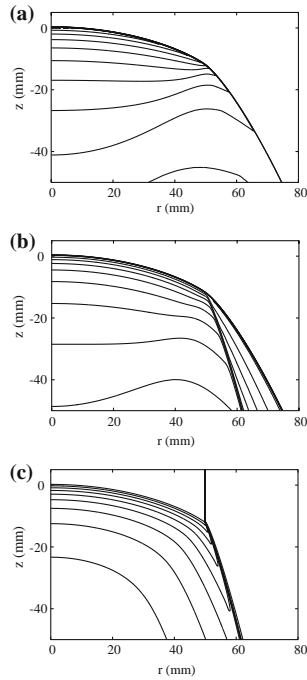

Figure 3. Numerical shock position based on cell in which pressure is maximum in axial direction for $\rho_I = 0\cdot8\,\text{g/cm}^3$, $d = 100\,\text{mm}$ and numerical resolutions, Δ, of (a) $0\cdot1\,\text{mm}$, (b) $0\cdot4\,\text{mm}$, (c) $0\cdot8\,\text{mm}$, (d) $3\cdot2\,\text{mm}$.

Figure 4. Contour plots of (a) pressure (contours of $0\cdot7$, $1\cdot1$, $1\cdot5$, $1\cdot9$, $2\cdot3$, $2\cdot7$, $3\cdot1$, $3\cdot5$, $3\cdot9$ and $4\cdot3$ GPa), (b) density (contours of $0\cdot6$, $0\cdot75$, $0\cdot9$, $1\cdot05$, $1\cdot2$, $1\cdot35$, $1\cdot5$, $1\cdot65$ and $1\cdot8\,\text{g/cm}^3$) and (c) reaction progress variable (contours of $0\cdot01$, $0\cdot1$, $0\cdot2$, $0\cdot3$, $0\cdot4$, $0\cdot5$, $0\cdot6$, $0\cdot7$ and $0\cdot8$), for $d = 100\,\text{mm}$ and $\rho_I = 0\cdot8\,\text{g/cm}^3$.

sonic locus is defined as the curve on which

$$M = \frac{\sqrt{u^2 + w^2}}{c} = 1,$$

where M is the local Mach number. Hence the region which governs the propagation of the front, or the detonation DDZ, is that between the shock and sonic locus. Note that close inspection of the near edge structures shows that for this case the sonic locus intersects the
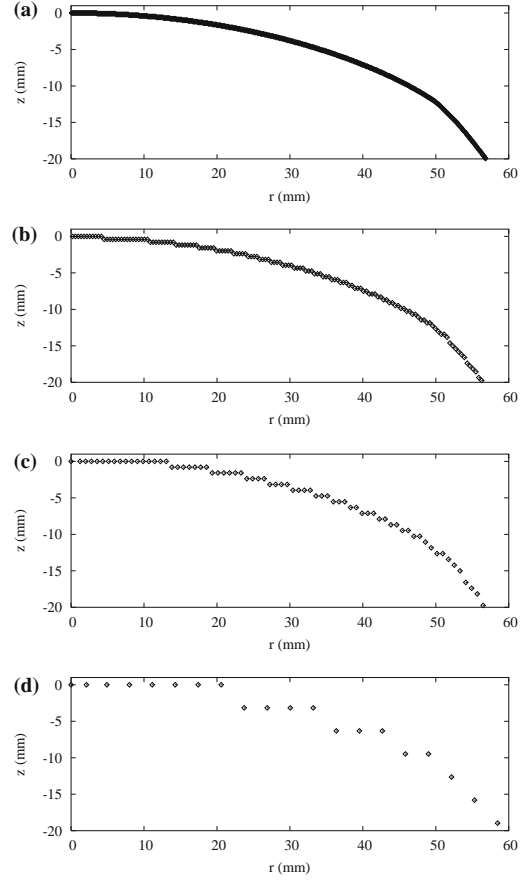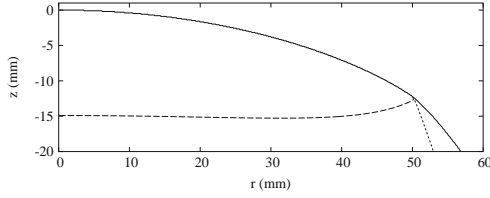
Figure 5. Shock locus (solid line), sonic locus (dashed line) and explosive/inert interface position (dotted line) for $d = 100\,\text{mm}$ and $\rho_I = 0\cdot8\,\text{g/cm}^3$.
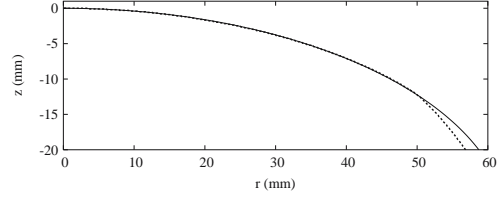

Figure 6. Shock locus (dotted line) for $d = 100\,\text{mm}$ and $\rho_I = 0\cdot8\,\text{g/cm}^3$, and ellipse of the form (5) with $\alpha = 31\cdot57$, $\beta = 63\cdot37$ (solid line).

explosive/inert interface very slightly below the shock front, and thus the post-shock flow in the explosive at the edge is slightly subsonic. Hence for this case the detonation is very weakly confined by the inert, since once the confinement is sufficiently weak that the flow at the edge becomes sonic, the DDZ becomes decoupled from the inert confiner because the flow along the explosive-inert interface is supersonic.

Note from Figure 4(c) that in this very weakly confined case, the burning does not proceed to completion in the steady wave. Figure 11(b) shows the axial profile of λ. The burning is effectively quenched in the expansion behind the sonic locus (λ asymptotes to $0\cdot9$ with distance behind the shock in this case). Note the pressure and hence reaction rate near the explosive–inert interface is much lower than at the axis. Hence as one approaches the interface a layer of only slightly burned material is formed (see Figure 4c). However, the quenching of the reaction rate occurs behind the sonic locus, and hence it is immaterial to the propagation of the front.

In order to examine the shape of the shock in the explosive, an ellipse of the form

$$\frac{(z+\alpha)^2}{\alpha^2} + \frac{r^2}{\beta^2} = 1 \tag{5}$$

was fitted through the shock locus data from the simulation. Figure 6 shows the comparison of an ellipse of the form in Equation (5) (with $\alpha = 31\cdot57$ and $\beta = 63\cdot37$) with the numerical shock locus, from which it can be seen that the ellipse can be fit very well to the locus in the explosive, *i.e.*, in the region $r \le 50\,\text{mm}$. Interestingly, it was found in [11] that experimental shock shapes in highly non-ideal explosives could also be well fitted to ellipses, which is not true for more ideal explosives [11].

5.1. Effect of charge diameter

Figure 8 shows the shock, interface and sonic loci when $\rho_I = 0\cdot8\,\text{g/cm}^3$, but now for larger charge diameters of 150 and 200 mm. The wave speed is $3\cdot73\,\text{km/s}$ ($0\cdot778D_{CJ}$) for $d = 150\,\text{mm}$, and $4\cdot02\,\text{km/s}$ ($0\cdot837D_{CJ}$) for $d = 200\,\text{mm}$. Again, in both cases an ellipse can be fitted well to the shock locus in the explosive. These fits show that the curvature of the shock at the axis decreases as d increases (see Section 5.3). Since the detonation speed increases with diameter, and hence the shock pressures and reaction rates also increase everywhere, the layer of partially burnt material near the explosive–inert interface becomes thinner. For $d = 150\,\text{mm}$, λ asymptotes to about $0\cdot97$ with distance along the axis, while for $d = 200$ the burning eventually proceeds all the way to completion.

A point to note from Figure 7 is that, although the detonation speed tends to the CJ speed and the front become less curved as d increases, the lag between the shock position at the axis and that at the edge *increases* with d. A similar result was found in [4] for the
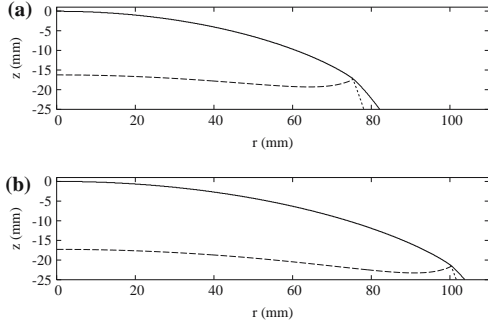
Figure 7. Shock locus (solid lines), sonic locus (dashed lines) and explosive/inert interface position (dotted lines) for $\rho_I = 0.8\,\text{g/cm}^3$ and (a) $d = 150\,\text{mm}$ and (b) $d = 200\,\text{mm}$.
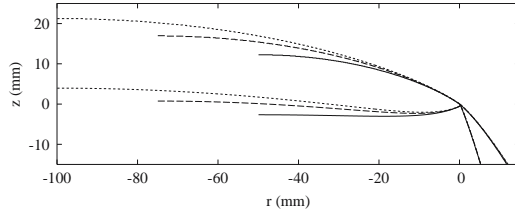

Figure 8. Shock, sonic and explosive/inert interface loci for $\rho_I = 0.8\,\text{g/cm}^3$ and $d = 100\,\text{mm}$ (solid lines), $d = 150\,\text{mm}$ (dashed lines) and $d = 200\,\text{mm}$ (dotted lines). In each case, the origin has been relocated to the point on the charge edge where the shocks and explosive–inert interface intersect.
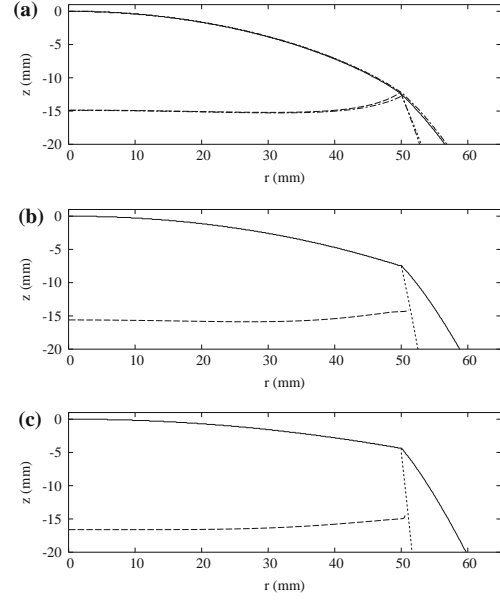

Figure 9. Shock locus (solid lines), sonic locus (dashed lines) and explosive/inert interface position (dotted lines) for $d = 100\,\text{mm}$ and (a) $\rho_I = 0.6\,\text{g/cm}^3$ (also shown as dot-dashed lines are the loci for $\rho_I = 0.8\,\text{g/cm}^3$), (b) $\rho_I = 2\,\text{g/cm}^3$ and (c) $\rho_I = 4\,\text{g/cm}^3$.

leading-order DSD theory, where it was shown that as $d \to \infty$, the lag in the edge shock position tends to infinity.

Figure 8 shows the loci (including the sonic loci) for the three diameters considered, $d = 100$, 150 and 200 mm, when $\rho_0 = 0.8\,\text{g/cm}^3$, but with the origin relocated to the shock/interface intersection point at the charge edge in each case. It can be seen that each of the shock, sonic and interface loci all overlay for the different diameters in a region within about 5 mm of the edge. Since Figure 8 shows the structure of all the loci sufficiently near the edge is not sensitive to d, this suggests that, for a given inert, a single simulation could be run for one diameter, and then the resulting near edge structure could be used to determine the near edge properties for other diameters without further simulations. This information could then be used in theoretical approaches to the two-dimensional steady detonation problem as edge boundary conditions, *e.g.* to determine diameter effects, without the need for further simulations.

Finally, note the qualitative change in the nature of the sonic locus as the diameter decreases. For larger d, the z-position of the locus has a local minimum at a radial position towards the charge edge. However, as d decreases, this minimum in the z-position becomes less pronounced. This agrees with the result in [18], where it was found that for sufficiently small diameters the sonic locus has no internal minimum in the axial position.

5.2. EFFECT OF CONFINEMENT

Figure 9 shows the shock, interface and sonic loci for a fixed diameter of $d = 100\,\text{mm}$, but for three different densities of the inert (0.6, 2 and 4 g/cm^3), giving different levels of confinement.

For $\rho_I = 0.6\,\text{g/cm}^3$, Figure 9(a) shows that the sonic locus and shock intersect at the charge edge. For comparison the base case (with $\rho_I = 0.8\,\text{g/cm}^3$) loci are also shown in Figure 9(a). For most of the charge radius the loci for the two cases are in good agreement. However, as the edge is approached they begin to diverge, especially the sonic loci. A result of this small difference in structures near the edge is that slightly less heat release occurs within the DDZ for $\rho_I = 0.6\,\text{g/cm}^3$ than in the base case, so that the axial speed is also slightly lower (3·11 km/s, as compared with 3·13 km/s for the base case). Note that since the flow is sonic at the edge behind the shock, this case can be considered to be 'unconfined' in that the DDZ is not in communication with the confinement as the flow along the interface is supersonic. Thus, any further decrease in the inert density does not affect the explosive DDZ (*e.g.* the axial speed or shock and sonic loci shapes of the steady detonation) [22], but as ρ_I decreases further there is an ever stronger Prandtl–Meyer fan embedded between the sonic locus and the interface [4]. A fit of an ellipse to the shock locus in the explosive for the unconfined case also shows that at the axis the shock is slightly more curved than as compared to the base case (see Table 2).

As ρ_I, and hence the degree of confinement increases for fixed d, the detonation tends to that of the planar CJ wave (the infinite confinement solution). Indeed, the detonation speed increases (see Table 2), and as can be seen in Figures 9(b, c), the shock front also becomes less curved, the sonic locus also becomes flatter and the post-shock flow in the explosive becomes increasingly subsonic at the edge, so that the distance between the shock and the sonic locus increases there. Thus, for a given diameter and sufficiently large ρ_I, the detonation will become close to CJ and hence the asymptotic DSD theories will become valid. Note also

Table 2. Properties of solution along the axis: D is the detonation speed; R_{shk} is the radius of curvature of the shock; p_{shk} is the shock pressure; p_{CJ} is the pressure at the sonic point; l_{DDZ} is the DDZ length (distance between shock and sonic point); l_{99} is the 99% reaction length (distance between shock and point where $\lambda = 0.99$); λ_{CJ} is the value of the reaction progress variable at the sonic point.

d (mm)	ρ_I (g/cm³)	D (km/s)	R_{shk} (mm)	p_{shk} (GPa)	p_{CJ} (GPa)
100	0·6	3·11	125·5	4·26	1·98
100	0·8	3·13	127·3	4·32	2·01
100	2·0	3·57	177·6	5·63	2·65
150	0·8	3·73	211·1	6·12	2·89
100	4·0	3·98	284·6	6·97	3·31
200	0·8	4·02	309·0	7·09	3·37
100	6·0	4·19	415·7	7·71	3·68
100	8·0	4·32	573·7	8·22	3·92

l_{DDZ} (mm)	l_{99} (mm)	λ_{CJ}
14·9	–	0·73
14·9	–	0·73
15·6	–	0·83
16·2	–	0·86
16·6	107·0	0·90
17·3	69·5	0·91
17·6	58·2	0·93
18·6	44·9	0·95

that the angle between the interface and the axis (*i.e.*, the flow deflection angle) decreases as the confinement increases. For these confined cases, ahead of the sonic locus the interface separates subsonic flow in the explosive from supersonic flow in the inert. Note that for fixed diameter and increasing confinement the local minimum in the *z*-position of the sonic locus moves towards the axis, and for high enough confinement the sonic locus slope becomes positive across the whole charge radius.

For the confined cases we find the shock front shape in the explosive can still be well fitted by the arc of an ellipse apart from a very small boundary layer region adjacent to the egde [4]. However, for very high confinements, such as the case with $\rho_I = 4\,\mathrm{g/cm^3}$ shown in Figure 9(c), the shock shape becomes too flat to be well represented on the grid at the resolution we are using.

5.3. Axial solution and quasi-one-dimensional analysis

Table 2 shows various properties of the axial solution for all of the cases which were simulated. These have been placed in order of ascending detonation speed in Table 2, from which it can be seen that the properties of the axial solution depend parametrically only on the axial detonation speed for both varying diameter and confinement (with the diameter or confinement serving to modify this speed). For example, Figure 10 shows the numerical data points for the axial radius of curvature of the shock (R_{shk}) against the detonation speed, which shows that all the data points appear to lie on a single curve. Hence as the detonation speed increases, the shock locus always becomes flatter at the axis. Also, Table 2 shows that, as expected, for higher detonation speeds the pressure throughout the reaction zone increases and hence the explosive burns more rapidly due to higher reaction rates. However, perhaps counter-intuitively, the axial DDZ length increases as the speed increases. This is due to the fact that, although the reaction rates are lower for smaller D, resulting in longer overall reaction lengths, the sonic point moves to an increasingly unburnt state (smaller λ_{CJ}) as D decreases (*cf.* [7]).

The fact that the axial solution depends only parametrically on the detonation speed (or alternatively on the radius of curvature of the shock at the axis), suggests that this dependence is governed by a simple D_n–κ law, *e.g.* as determined by a quasi-one-dimensional analysis.

Here we determine if the numerical results do indeed agree with such a quasi-one-dimensional theory. In order to perform such an analysis, the steady Reactive Euler equations are first transformed from (r, z) coordinates to a shock-attached coordinate system (n, ξ) where n is the normal distance of any point from the shock (with positive (negative) values corresponding to points ahead (behind) the shock) and ξ is the arclength along the shock (measured from the charge axis).

In such a co-ordinate system, the governing equations transform to

$$\frac{\partial(\rho u_n)}{\partial n} + \frac{\kappa \rho(u_n + D_n)}{1 + n\kappa} = R_1, \quad u_n \frac{\partial u_n}{dn} + \frac{1}{\rho}\frac{\partial p}{\partial n} = R_2, \quad \frac{\partial e}{\partial n} - \frac{p}{\rho^2}\frac{\partial \rho}{\partial n} = R_3, \quad \frac{\partial \lambda}{\partial n} - \frac{W}{u_n} = R_4, \quad (6)$$

where $\kappa(\xi)$ is the curvature of the shock and $D_n(\xi)$ is the normal component of the shock speed, at an arclength of ξ from the axis along the shock, while u_n is the component of material velocity in the n direction. R_1 to R_4 contain terms involving partial derivatives with respect to ξ or involving u_ξ, the component of the material velocity in the ξ-direction (these terms are given in [23] or [24]).

The quasi-one-dimensional approximation is then that the variables vary slowly in the ξ-direction along the shock, *i.e.*, that the ξ-derivative terms in R_1 to R_4 are negligible. If this approximation is valid, the variables depend, to leading order, only parametrically on
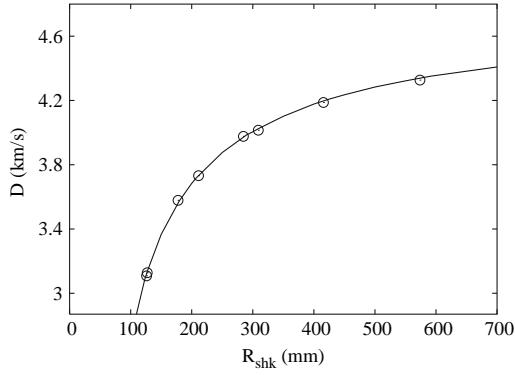
Figure 10. Axial detonation speed versus axial radius of curvature of the shock. Circles are data points from numerical simulations. The solid line is the D_n–R relation from the quasi-one-dimensional analysis.
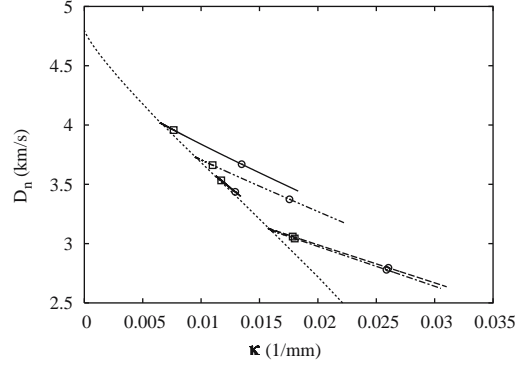

Figure 12. Normal detonation speed against curvature along individual shock loci for $d = 100$ mm, $\rho_I = 0\cdot8$ g/cm³ (dashed line), $d = 100$ mm, $\rho_I = 0\cdot6$ g/cm³ (dot-dashed line), $d = 150$ mm, $\rho_I = 0\cdot8$ g/cm³ (double-dot-dashed line), $d = 200$ mm, $\rho_I = 0\cdot8$ g/cm³ (triple-dot-dashed line), $d = 100$ mm, $\rho_I = 2$ g/cm³ (solid line). The dotted line is the quasi-one-dimensional $D_n - \kappa$ relation. The squares and circles mark the points where r is 50% and 90% of the charge radius, respectively.

Figure 11. Axial profiles of (a) pressure and (b) reaction progress variable against distance from the quasi-one-dimensional theory with $R = 127\cdot3$ mm (solid line) and from numerical simulation with $d = 100$ mm, $\rho_I = 0\cdot8$ g/cm³ (dashed line).

ξ through the values of $\kappa(\xi)$ and $D_n(\xi)$. The reduced form of Equations (6) can then be manipulated into the form

$$\frac{d\rho}{dn} = \frac{-Q(\gamma - 1)\rho W/u_n + \kappa^*\rho u_n(u_n + D_n)}{c^2 - u_n^2},$$

$$\frac{du_n}{dn} = \frac{Q(\gamma - 1)W - \kappa^*c^2(u_n + D_n)}{c^2 - u_n^2}, \quad \frac{d\lambda}{dn} = \frac{W}{u_n}, \quad (7)$$

where $\kappa^* = \kappa/(1 + n\kappa)$, c is given by Equation (4) and

$$p = \frac{(\gamma - 1)\rho}{\gamma}\left[\frac{D_n^2 - u_n^2}{2} + Q\lambda\right]. \quad (8)$$

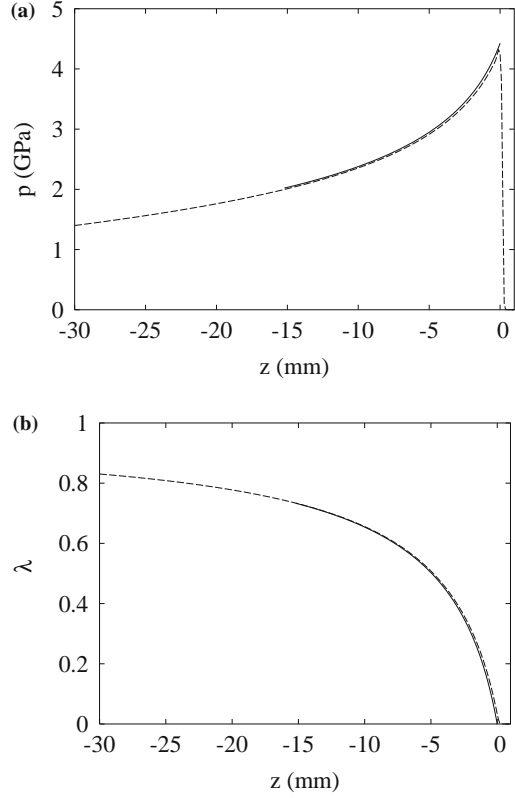(note that the strong shock approximation has been used to derive Equation (8))

Hence Equations (7) are a set of three ordinary differential equations in three unknowns (ρ, u_n and λ). These are subject to the shock jump conditions, which determine the values of ρ, u_n at the shock for a given value of D_n (note $\lambda = 0$ behind the shock), and to a generalized CJ or compatibility condition that the numerator in the right-hand side of the first two of Equations (7) are zero when the flow is sonic (*i.e.*, when the denominator is simultaneously zero). The resulting boundary-value problem is thus an eigenvalue problem for D_n (for fixed κ). The numerical shooting method for solving this problem is described in [7] and [8]. By varying κ one can then map out a quasi-one-dimensional D_n–κ relation. Note that here no assumption has been made regarding the size of κ.

Specializing to the axis, the axial radius of curvature is related to the curvature by $R_{shk} = 2/\kappa$ and hence one can instead determine a quasi-one-dimensional (Q1D) $D_n - R_{shk}$ relationship, which is shown in Figure 10. Note that the numerical simulation data points in Figure 10 are all in excellent agreement with the quasi-one-dimensional theory, indicating that the Q1D approximation holds very well for the axial solution, but importantly note also that the Q1D is not exact on the axis, one term in R_1 is not zero there [13], however higher-order DSD analysis indicate this term is numerically small on the axis (J. Bdzil, private communication). Indeed, our results show this term has little influence on the axis, even when the detonation speed is significantly below the CJ speed. Figure 11 also shows a comparison between the axial pressure and λ profiles from the base case simulation, with that predicted by the Q1D theory using the axial shock radius of curvature determined from the simulation, from which it can be seen that the Q1D solution gives excellent agreement with the axial solution from the simulations.

The fact that, given the axial radius of curvature of the shock, the Q1D theory gives accurate predictions of the detonation speed and the axial solution, even for highly non-ideal detonations, is an important result because in industry Wood-Kirkwood codes tend to be used for such predictions. However, WK theory is incomplete since, even given R_{shk}, the theory contains an unknown function, namely the axial flow divergence $(\partial u/\partial r)_{r=0}$, about which some assumption needs to be made. In terms of the version of the WK theory presented for example in [25], on the axis the Q1D theory is directly related to the WK theory: the unknown flow divergence term in WK is simply replaced by the appropriate Q1D curvature term. However, typically industrial versions of WK theory involve an additional variable and equation (the 'central stream tube area'), as well as further assumptions [1], than in the simpler form in [25]. Hence the Q1D theory is actually a simpler system to solve than in these industrial WK theories, with fewer governing equations, but it is also less obvious how the two are directly related in this case. Note that for a given explosive model, the Q1D theory is still incomplete in that, as in WK theory, one still needs to make some assumptions about how R_{shk} is dependent on the charge diameter and confinement. However, given such an assumption, the Q1D theory has no other unknowns, and hence avoids the main uncertainty in WK theory (namely the unknown axial flow divergence function). Finally, in the Q1D approximation we have made no assumptions about the flow being weakly curved (or slightly divergent), instead the full Q1D equations have been solved numerically for arbitrary R_{shk} (or κ). As can be seen from Figure 10, this Q1D theory gives very good results even at detonation speeds significantly below the CJ speed. Hence, given a reaction rate and an eos model, the Q1D theory offers a significant improvement to WK codes currently used in defence and commercial industries.

5.4. D_n–κ SHOCK LOCI RELATIONS

We now investigate the validity of the Q1D approximation off-axis. Note that, since we have found that the steady detonation shock loci are well approximated by arcs of ellipses, one can

analytically construct D_n and κ at each point on the shock front from these fits, and hence obtain a D_n–κ relationship for individual shock loci.

If the Q1D approximation holds off-axis then the D_n–κ relation along an individual shock locus should be in good agreement with the Q1D relation. Figure 12, which shows the D_n–κ curves along individual shock loci from various numerical simulation runs as well as the Q1D D_n–κ relation, reveals this is not the case. While the shock loci curves all intersect the Q1D curve at $r = 0$, their slopes are different to that of the Q1D relation. Furthermore, individual shock loci for different confinements and diameters all lie along different curves. Hence the Q1D approximation does not hold off axis, and ξ derivatives must be important for $\xi > 0$.

This behaviour is in agreement with experimental shock shapes for highly non-ideal explosives. Indeed, despite the fact that we have used a simple model, the shock shapes in the D_n–κ plane are in remarkable agreement with the experimental figures in [11] and [15] for ANFOs. Also shown in Figure 12 are markers which show where the points corresponding to 50% and 90% across the charge radius lie, from which it can be seen that most of the D_n–κ variation along the shock front occurs closer to the edge than to the axis.

The confined case with $\rho_I = 2\,\text{g/cm}^3$ shown as a solid line in Figure 12 agrees better with the Q1D result than for the weakly or unconfined cases for the same charge diameter. Indeed, for the confined case shown, the curvature variation across the charge is much smaller than for the weakly confined cases, showing that variations with ξ become less pronounced for higher confinements (as the degree of confinement increases further, the calculated shock shapes occupy a smaller and smaller region in the D_n–κ plane). Hence the terms neglected in Equations (6) involving arc-length variations become smaller and thus the Q1D approximation becomes better, as expected.

6. Conclusions

In this paper we have used simple eos and rate-law models to perform numerical simulations of steady detonations in cylindrical charges of non-ideal explosives. It was shown that very high resolutions, typically an order of magnitude larger than used in engineering simulations, are required for accurate (well converged) numerical results (for the detonation speed, shock shapes, etc.), even when such simple rate and eos models are used. For pressure-dependent rate-law models, as used here, where the reaction rate is maximum at the shock front, burning in the numerically smeared shock is an issue even for reasonably high resolution.

We then used high-resolution simulations to examine the qualitative dependence of the two-dimensional steady solution on the charge diameter and the degree of confinement. For our model, we found that the shock-shapes could be fitted well to an arc of an ellipse, with good agreement with experimental shock shape dependencies. We also found that the axial solution from the numerics depended parametrically on the radius of curvature of the shock at the axis, with charge diameter or confinement serving to modify the axial curvature. These axial results agreed very well with an approximate quasi-one-dimensional theory, even for highly non-ideal detonations which propagate significantly below the Chapman-Jouguet speed. This quasi-one-dimensional theory therefore offers an improvement over industrial Wood-Kirkwood codes, both in terms of accuracy and mathematical simplicity.

In this paper we have used a simple confinement model since our purpose was only to examine how different levels of confinement affect the detonation wave and its structure. However, in many applications one is also interested in how the passage of the detonation affects a specific inert confiner, including confining layers of small thickness in the radial direction. In these cases the eos for the inert model may be markedly different from that of

the explosive, and then simple capturing of the interface as has been done here and in previous works is no longer viable. Instead the interface must usually be tracked in some way. However, the applicability and numerical issues involved with different tracking algorithms for these types of reactive–inert interface problems do not appear to have been properly studied (indeed 'closure' issues are known to exist). We intend to examine the strengths and weaknesses of different tracking algorithms when applied to these detonations problems in the future.

However, in the case where the confiner is sufficiently strong, one can perform an asymptotic analysis of how the confiner reacts to a given pressure loading along the interface, including the dependence on the inert thickness (Sharpe and Bdzil, submitted). This analysis essentially provides the coupling condition between the pressure loading and the shape of the deflected inert. Currently, we are working on using this coupling condition to develop a complete asymptotic solution to the fully coupled explosive–inert interaction problem. This includes a DSD approximation for the detonation in the interior of the explosive, but which includes boundary layers adjacent to the interface where the DSD approximation breaks down, and also for the deflection of the confiner.

We have also used simple eos and rate-law models calibrated to an ANFO-like material in this paper. More complex semi-empirical rate-law and eos models exist for different types of explosives, but performing fully resolved simulations with such models can increase the computational cost dramatically. Indeed, typically these more complex models have only be used for highly unresolved hydrocode simulations, but proper mathematical analysis of the solutions and properties of these models, or even resolved simulations of the steady-state detonation problem, are generally lacking. It is hence necessary to begin examining these points more throughly by building a hierarchy of models of increasing complexity and examining their applicability. A proper study and analysis of existing models is currently underway at LANL.

Finally, here we have only considered the final steady-state solution. Another point of interest is the evolution from various initial (initiation) conditions to the steady state, including run-up distances (the distance the shock travels from the initiation site to the achievement of steady state). It would also hence be worth examining this evolution using simulations of different initiation processes.

Appendix A: Additional results

In the main body of the text, the results were given for eos and rate-law parameter choices that were calibrated to an ANFO-like material. However, simulations for several different parameter choices were additionally ran for the widely used simple class of model with weakly pressure-dependent rate law of the form $kp^n(1-\lambda)^m$ and pseudo-polytropic eos $e = p/((\gamma^* - 1)\rho)$, to ensure our the main points and conclusions were not sensitive to the specific choice of parameters. This was indeed found to be the case. For example, Figures 13 and 14 show some additional results for $n=1$, $m=1/2$, $\gamma^*=3$ (*i.e.*, for a different choice of both the rate and eos parameters than used in Section 5). The point to note from these figures is that the main results and conclusions described in Section 5 also apply for a different choice of the rate and eos parameters. (NB. since we are not calibrating to a specific explosive for these parameters, the results have been left in dimensionless form, where the characteristic velocity is the CJ speed, the characteristic density is the initial explosive density ($\rho_0 = 1$ in dimensionless units) and the characteristic length is the standard half-reaction length, *i.e.*, the distance
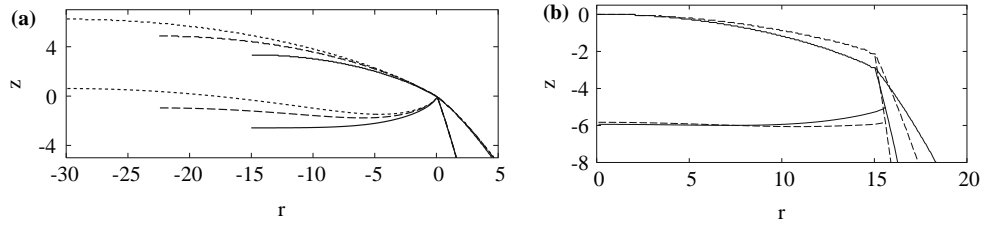
Figure 13. Shock, sonic and explosive/inert interface loci for $n=1$, $m=1/2$, $\gamma^*=3$ and (a) $\rho_I=1$ and $d=30$ (solid lines), $d=45$ (dashed lines) and $d=60$ (dotted lines) (the origin has been relocated to the point on the charge edge where the shocks and interface intersect) and (b) $d=30$ with $\rho_I=2$ (solid lines) and $\rho_I=5$ (dashed lines).
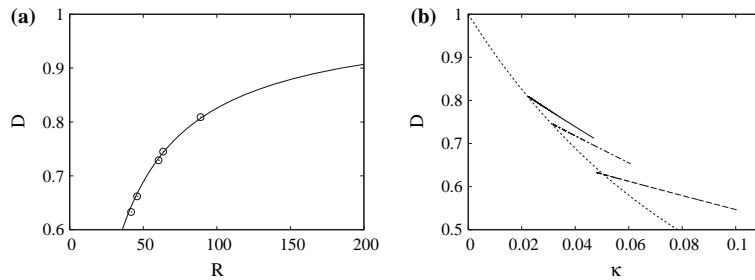

Figure 14. (a) Axial detonation speed versus axial radius of curvature of the shock from Q1D D_n-R relation (solid line) and from numerical simulations (circles), and (b) $D_n-\kappa$ relation from Q1D theory (dotted line) and along individual shock loci for $\rho_I=1$ and $d=30$ (dashed line), 45 (dot-dashed line) and 60 (solid line), when $n=1$, $m=1/2$, $\gamma^*=3$.

between the shock and the point where $\lambda=0\cdot5$ in the ZND wave). The resolution was of the order of 100 points in the axial DDZ.

Acknowledgements

References

1. I.J. Kirby and G.A. Leiper, A small divergent detonation theory for intermolecular explosives. In: *8th Symp. (Int.) on Detonation.* Arlington: Office of Naval Research (1985) pp. 176–186.
2. W.M. Howard, L.E. Fried, P.C. Souers and P.A. Vitello, Calculation of chemical detonation waves with hydrodynamics and a thermochemical equation of state. In: M.D. Furnish, N.N. Thadhani and Y. Horie, (eds), *Shock Compression of Condensed Matter.* American institute of Physics (2001) pp. 161–164.
3. W.W. Wood and J.G. Kirkwood, Diameter effect in condensed explosives - the relation between velocity and radius of curvature of the detonation wave. *J. Chem. Phys.* 22 (1954) 1920–1924.
4. J.B. Bdzil, Steady-state two-dimensional detonation. *J. Fluid Mech.* 108 (1981) 195–266.
5. J.B. Bdzil and T.D. Aslam, Detonation front models: theories and methods. Los Alamos: Los Alamos National Laboratory Report LA-UR-02-942 (2000) 51 pp.

6.   J.B. Bdzil., W. Ficket and D.S. Stewart, Detonation shock dynamics: a new approach to modeling multi-dimensional detonation waves. In: *9th Symp. (Int.) on Detonation*. Arlington: Office of Naval Research (1989) pp. 730–742

7.   G.J. Sharpe, The effect of curvature on pathological detonations. *Combust. Flame* 123 (2000) 68–81.

8.   G.J. Sharpe, The structure of planar and curved detonation waves with reversible reactions. *Phys. Fluids* 12 (2000) 3007–3020.

9.   T.D. Aslam and J.B. Bdzil, Numerical and theoretical investigations on detonation-inert confinement inter-actions. In: *12th Symp. (Int.) on Detonation*. Arlington: Office of Naval Research (2002) in print.

10. L.G. Hill, J.B. Bdzil and T.D. Aslam, Front curvature rate stick measurements and detonation shock dynamics calibration for PBX 9502 over a wide temperature range. In: *11th Symp. (Int.) on Detonation*. Arlington: Office of Naval Research (1998) pp. 1029–1037

11. D.L. Kennedy, Multi-valued normal shock velocity versus curvature relationships for highly non-ideal explo-sives. In: *11th Symp. (Int.) on Detonation*. Arlington: Office of Naval Research (1998) pp. 181–192.

12. L.G. Hill, J.B. Bdzil, W.C. Davis and R. Engelke, Front curvature analysis and detonation shock dynamics calibration fro pure and sensitized nitromethane. In: M.D. Furnish, L.C. Chhabildas and R.S. Hixson (eds), *Shock Compression of Condensed Matter*. American institute of Physics (1999) pp. 813–816.

13. T.D. Aslam, J.B. Bdzil and L.G. Hill, Extensions to DSD theory: analysis of PBX 9502 rate stick data. In: *11th Symp. (Int.) on Detonation*. Arlington: Office of Naval Research (1998) pp. 21–29.

14. R.A. Catanach and L.G. Hill, Diameter effect curve and detonation curvature measurements for ANFO. In: M.D. Furnish, N.N. Thadhani and Y. Horie (eds), *Shock Compression of Condensed Matter*, American institute of Physics (2001) pp. 906–909.

15. J.B. Bdzil, T.D. Aslam, R.A. Catanach, L.G. Hill and M. Short, DSD front models: non-ideal explosive detonation in ANFO. Los Alamos: Los Alamos National Laboratory Report LA-UR-02-4332 (2002) 11 pp.

16. D.S. Stewart and J. Bdzil, The shock dynamics of stable multidimensional detonation. *Combust Flame* 72 (1988) 311–323.

17. P.C. Souers, R. Garza and P. Vitello, Ignition and growth and JWL++ detonation models in coarse zones. *Propell., Expl., Pyrotech.* 27 (2002) 62–71.

18. V.N. Gamezo and E.S. Oran, Reaction-zone structure of a steady-state detonation wave in a cylindrical charge. *Combust. Flame* 109 (1997) 253–265.

19. J.F. Clarke, S. Karni, J.J. Quirk, P.L. Roe, L.G. Simmonds and E.F. Toro, Numerical computation of two-dimensional unsteady detonation waves in high energy solids. *J. Comp. Phys.* 106 (1993) 215–233.

20. T.L. Freeman, I. Gladwell, M. Braithwaite, W. Byers Brown, P.M. Lynch and I.B. Parker, Modular software for modelling the ideal detonation of explosives. *Math. Engng. Ind.* 3 (1991) 97–109.

21. G.J. Sharpe and S.A.E.G. Falle, One-dimensional nonlinear stability of pathological detonations. *J. Fluid Mech.* 414 (2000) 339–366.

22. G.J. Sharpe, Supplement to HSBM research report on rate stick simulations. Hybrid Stress Blast Model Pro-ject research report (2004) 5 pp.

23. J. Yao and D.S. Stewart, On the dynamics of multi-dimensional detonation, *J. Fluid. Mech.* 309 (1996) 225–275.

24. M. Short and J.B. Bdzil, Propagation laws for steady curved detonations with chain-branching kinetics. *J. Fluid. Mech.* 479 (2003) 39–64.

25. W. Fickett and W.C. Davis, *Detonation*. Berkeley: University of California Press (1979) 386 pp.